Forming limit diagram of annealed copper OFE thick sheets for optimized hydroforming of superconducting RF cavities

Adrià Gallifa-Terricabras [a], Joanna Sylwia Swieszek [a,b], Dorota Smakulska [a], Berta Ruiz-Palenzuela [a], Marco Garlaschè [a]

[a] *CERN European Organization for Nuclear Research, Espl. des Particules 1, Geneva 1211, Switzerland*
[b] *Kraftanlagen Nukleartechnik GmbH, Im Breitspiel 7, Heidelberg 69126, Germany*

A R T I C L E   I N F O

A B S T R A C T

Coated superconducting radio-frequency (SRF) cavities are planned to be implemented in the Future Circular Collider (FCC) at the European Organization for Nuclear Research (CERN). The interest in industrialized and high-performance processes for fabrication of the corresponding copper substrates has thus risen. Tubular hydroforming is a well-known industrial process, but has not been thoroughly applied for ultra-pure oxygen-free electronic copper (Cu-OFE) thick products. To provide a feasibility analysis for the optimized fabrication process of copper substrate seamless cavities, a Forming Limit Diagram (FLD) of the material of interest was studied. In this paper, the methodology, test results and initial benchmark of the material model is presented, for 4 mm and 2 mm thick sheets.

1. Introduction

The manufacturing of superconducting radio-frequency (SRF) elliptical cavities for particle accelerators typically involves large deformation processes (e.g. deep drawing, spinning, hydroforming) of pure copper or pure niobium sheet-like products. Cavities made of spun Cu half-cells welded along the equator and coated with a Nb thin film (Nb/Cu) were developed and employed at CERN in the LEP project [1], and are currently being operated in the CERN Large Hadron Collider (LHC); if compared to bulk niobium, these coated cavities provide increased thermal stability while offering significant cost savings for series production [1]. Also due to such cost effectiveness considerations, Cu substrates fall within the baseline for the Future Circular Collider (FCC) [2]. The possibility of eluding a circumferential weld in correspondence with the equator of elliptical cavities, can drive further reduction of fabrication costs, while also allowing for enhanced SRF performance. Consequently, extensive research is being conducted to improve the techniques for coating copper substrates with niobium (Nb) or niobium-tin (Nb$_3$Sn) thin films [3], [4], [5], [6], [7].

For many years, hydroforming (HF) has been regarded as a promising process for jointly meeting the requirements of RF performance and cost reduction. Previous attempts to obtain single or multi-cell cavities from a tube have been carried out by different high energy-physics laboratories

worldwide. Notable efforts include those by researchers at CERN [8], by KEK [9], as well as subsequent work by teams at DESY [10] and [11]. These endeavors have encountered numerous challenges, particularly due to the need of achieving good precision and surface quality, while mastering multiple steps of large deformation. The activities discussed in this study are part of a broader campaign conducted by the authors and their team at CERN, focusing on modeling and characterizing large deformation processes employed in the fabrication of components for particle accelerators [12] [13].

Specifically, in the case of elliptical seamless SRF cavities, the combination of advanced process simulations utilizing finite element modeling (FEM), innovative material characterization techniques, and reliable fabrication methods can potentially pave the way for optimizing production through hydroforming (i.e., obtaining the final cavity shape with the least number of forming steps and intermediate annealing steps). To assess the feasibility of a process through FEM simulations, precise models of the mechanical behavior and material-specific failure models are required. These models should accurately define the formability and failure limits of the initial products, subjected to significant deformations in the case under investigation.

The analysis of in-plane true strains in the Forming Limit Diagram (FLD) is still the most established method for failure detection of sheet metal forming processes in industrial practice; this approach has proved
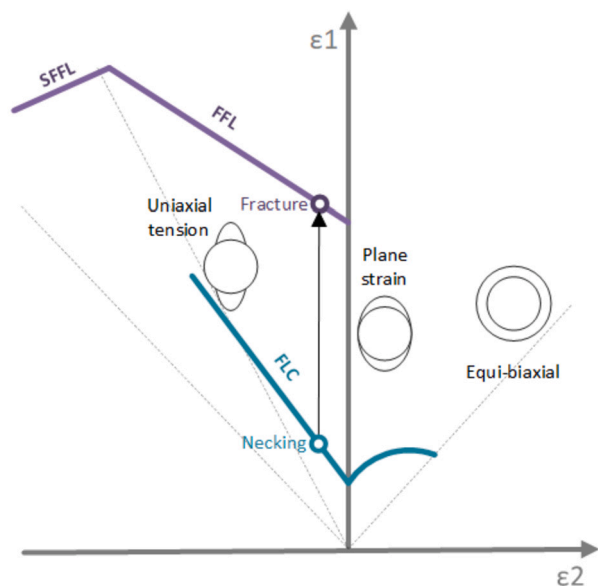
Fig. 1. Schematic Forming Limit diagram (FLD) containing an arbitrary Forming Limit Curve (FLC), which represents the onset of necking in the material, and the Fracture Forming Limit (FFL) together with the Shear Fracture Forming Limit (SFFL), representing where the ultimate failure occurs.

Table 1
Chemical composition of the 4 mm thick Cu–OFE sheet from the material certificate (type 3.1 acc. to EN 10204). All values are expressed in weight ppm except Cu which is in weight%. The measurements were obtained by spark and gas optical emission spectrometry.

Cu		Ag	As	Bi	Cd	Fe	Mn	Ni
99.996		11.4	1.8	0.6	0.4	1.2	< 0.2	3.5
O	P	Pb	S	Sb	Se	Sn	Te	Zn
1.3	< 0.3	1.3	6.8	1	0.9	< 0.7	< 2	< 0.1

Table 2
Grain size and Vickers hardness measurements of the Cu–OFE 2 mm and 4 mm thick sheets, before and after heat treatment. Load force for the HV tests was set to 100 g, values reported are average value and standard deviation of 5 measurements.

Sheet Thickness	Condition	G ASTM E112 (equivalent diameter in μm)	Hardness, $HV_{0.1}$
4 mm	As-received (1/2 hard)	G8 (22 μm)	95 ± 3
4 mm	Annealed (2 h at 600 °C in vacuum)	G6 (44 μm)	45 ± 4
2 mm	As-received (1/2 hard)	G7.5 (26 μm)	81 ± 6
2 mm	Annealed (2 h at 600 °C in vacuum)	G5.5 (52 μm)	49 ± 0

valid for strain paths which remain linear during the deformation process [14] [15]. FLDs for pure copper and copper alloys of reduced thickness (less than 1 mm) exist in the literature [16], as well as Cu OFE mechanical characterization in the context of SRF [17]. However, forming limit diagrams for oxygen-free electronic copper (Cu–OFE) and for increased thickness (above 1 mm) have not yet been explored in detail and will be the subject of this paper.

FLDs for 2 mm and 4 mm thick Cu–OFE sheets are obtained thanks to a simplified approach, by performing tensile tests on two specimen geometries leading to uni-axial and quasi plane-strain paths. The validity of the specimens geometry has been benchmarked with FEM simulations. The presented results focus mainly on the strain domain between uni-axial and plane-strain deformation paths (corresponding to the 2nd quadrant of the FLD) which appears to be the region of interest for optimal forming (less thinning, wrinkles avoidance, higher forming limit).

For completeness, the obtained FLD results have been compared with theoretical models. For general illustration purposes, Fig. 1 presents a typical FLD, containing information on the onset of necking (i.e. forming limit curve, FLC) and also on the Fracture Forming Limit (FFL, corresponding to the rupture of the material) and on the Shear Fracture Forming Limit (SFFL, rupture in the shear region).

2. Materials and methods

2.1. Preparation and characterization of Cu–OFE sheets

2 mm and 4 mm thickness copper–OFE sheets in half-hard temper state (H02) were used (material purchased according to ASTM B152, ASTM F68 and EN 13604). These thicknesses were selected to represent a common value after forming steps and a typical starting thickness for SRF applications. Specimens were extracted by micro water jet cut: on one hand for the preliminary material characterization (hardness, grain size, tensile mechanical properties) and on the other hand, for the construction of the FLD through tensile tests employing Digital Image Correlation. After extraction and prior to testing, the specimens were subjected to a heat treatment at 600 °C under vacuum ($< 1.10^{-5}$ mbar) for 2 hours, in order to achieve a soft annealed state. With such treatment, the yield strength of the material is reduced with respect to the ultimate strength, while elongation at break is increased, thus increasing the formability of the material.

The chemical composition of the Cu–OFE raw material (values from the material certificate type 3.1 acc. to EN-10204) is shown in Table 1. Table 2 provides the summary of grain size and hardness measurements (obtained according to ASTM E112 and to ISO 6507–1 respectively) performed on as-received and after heat treatment specimens.

Representative microstructure images of the as-received and the heat-treated 4 mm thick sheet are shown in Fig. 2.

For the simplified FLD construction, the two specimen geometries presented in Fig. 3 were employed; these are designated as "UA" for uni–axial and "PS" for plane–strain, and are extracted with their main axis parallel to the sheets longest direction (assumed to be the sheet rolling direction), hereafter referred as 0 degree orientation. The "UA" specimen geometry is in accordance with the ASTM E8 subsize specimen (this geometry was also employed for the preliminary tensile tests), whereas the PS specimen geometry was adapted from [18] to fit with the hydraulic gripping wedges of the universal mechanical testing machine used for the tests (Zwick Z250, ZwickRoell GmbH). For each thickness (i.e. 2 mm and 4 mm) three specimens were tested for the UA condition, and two for PS condition. Additional 2 mm thickness UA specimens were cut at 45 and 90 degrees with respect to the sheet longest direction, in order to assess the planar anisotropy. For the preliminary tensile tests, the axial deformation was monitored by means of video–extensometer, while for the FLD construction, a Digital Image Correlation (DIC) system (Q400-3D, Limess Messtechnik und Software GmbH) was also employed.

The strain rate of the tests was set to 0.015 1/s. Such value is in line with the strain rate values to which the material is submitted during HF process; the HF strain rate values have been benchmarked through FEM simulations, considering an axial advancement of the hydroforming dies equal to 1 mm/s, typical for such process. Cu–OFE is rather insensitive to strain rate variations up to 10^3 s^{-1} [17], which is largely within the range applicable to the HF process under study. This leads to the assumption that the chosen strain rate is valid for this study and similar low strain rate deformation processes. However, for high strain rate applications, such as explosion forming, dedicated FLD tests at corresponding strain rates are recommended.

A pre–load of 3 MPa was applied. For the DIC, a stochastic pattern was applied to the specimens surface, consisting of a base layer of acrylic matte white paint with a graphite black paint speckle. The acquisition frequency was kept in the range of 10 – 15 Hz in order to obtain between 400 and 600 valid frames for a single test. The facet-size used
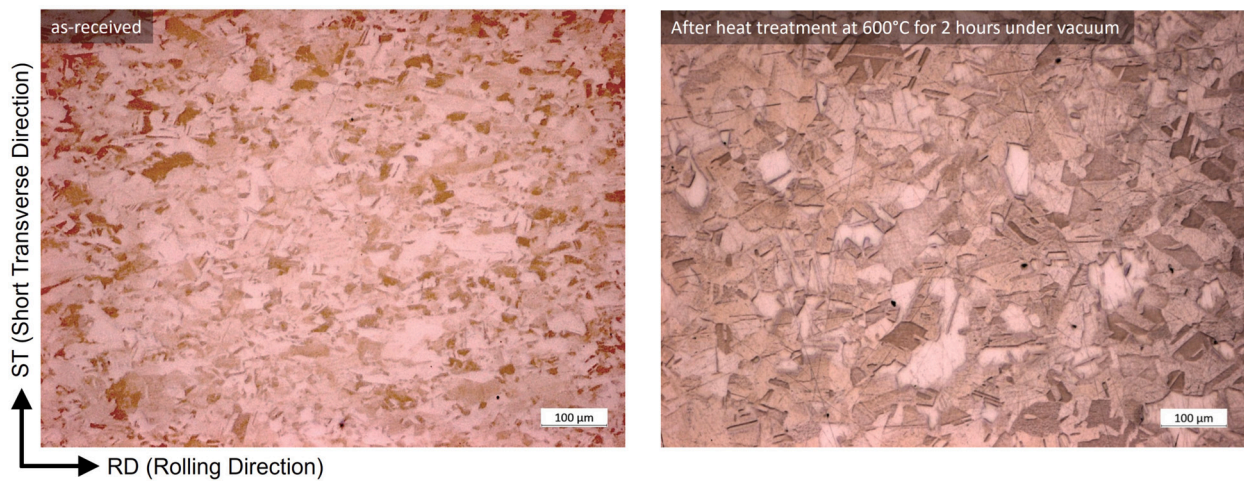
Fig. 2. Representative microstructure images of the as-received (half-hard) and heat-treated (600 °C, 2 h, under vacuum) Cu OFE 4 mm thick sheet. Etched in a 50% vol. nitric acid-water solution. Original magnification: 100x.
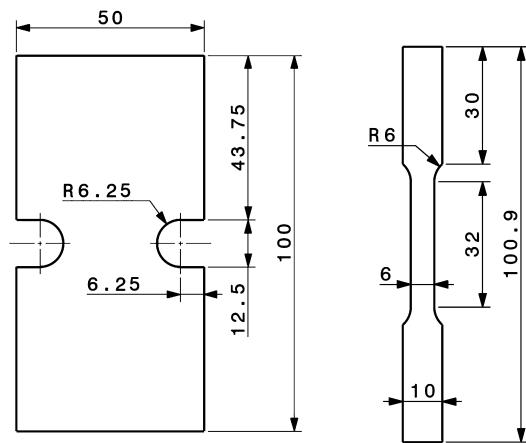

Fig. 3. Schematic drawings for specimens subjected to plane strain "PS" (left) and uni-axial "UA" strain paths (right). Dimensions in mm.

Table 3

Tensile test results for 4 mm thick Cu-OFE annealed sheets. Values shown are the average and one standard deviation from 3 specimens. Key: $R_{p0.2}$: Yield strength at 0.2% offset, $R_{p1.0}$: Yield strength at 1.0% offset, R_m: Ultimate tensile strength, A_g: Total elongation at maximum force, A_{25mm}: Elongation at break (on a 25 mm gauge length), $\frac{R_{p0.2}}{R_m}$: Ratio of $R_{p0.2}$ to R_m, $n_{0.02-0.20\text{ true strain}}$: Strain hardening exponent (calculated over true strain range from 0.02 to 0.20).

Orientation w.r.t. sheet long direction	$R_{p0.2}$ (MPa)	$R_{p1.0}$ (MPa)	R_m (MPa)	A_g (%)
0 degrees	32.0 ± 0.8	41.2 ± 0.8	226.5 ± 0.2	37.6 ± 0.6

Orientation w.r.t. sheet long direction	A_{25mm} (%)	$\frac{R_{p0.2}}{R_m}$ (%)	$n_{0.02-0.20\text{ true strain}}$ (-)
0 degrees	63.7 ± 0.8	14.1 ± 0.4	0.535 ± 0.003

ranged from 25 to 29 pixels (corresponding to about 1.5 mm) and the grid spacing (distance between facets centers) was set between 7 and 10 px (corresponding to 0.5 mm). These parameters allowed to obtain a certain overlap for each analyzed sub-element. The experimental setup is shown in Fig. 4 and consists of two cameras (2 MegaPixel, 50 mm focal length) connected to a DAQ system and a PC equipped with ISTRA 4D software for image acquisition, target calibration and images/data post-processing.

Unless explicitly specified, the strain values presented below are consistently expressed in true values, to facilitate direct comparison and exploitation of the results with FEM simulations. The measured material properties derived from the preliminary tensile tests are shown in Table 3 for 4 mm thick specimens and in Table 4 and Table 5 for the 2 mm thick specimens. The curves obtained in the experiment are presented in Fig. 5 and Fig. 6 for 4 mm thick specimens (specimens cut with its longest dimension parallel to the longest dimension of the sheet, i.e. 0 degree angle) and in Figs. 7 and 8 for 2 mm thick specimens (specimens cut with its longest dimension with at an angle of 0, 45 and 90 degrees with respect to the longest dimension of the sheet).

For the purchase of copper tubes for hydroforming, they should be delivered in soft annealed state (O60) in accordance with ASTM B188, or in the R200 material condition in accordance with EN 13600. However, since the minimum yield strength is not defined in these standards, it is recommended to request the lowest achievable value to obtain maximum formability, comparable to the material condition in this study. If

the material is delivered in a hardened state, an initial annealing would be required to achieve maximum formability. Regarding grain size, it is recommended to purchase a product with the smallest possible size to minimize the 'orange peel' effect upon deformation, which might affect the quality of the thin film coating.

2.2. Validation of specimen geometry by FEM simulations

The maximum and average strain ($\varepsilon 1$ and $\varepsilon 2$) -recorded by DIC in a square of 4x4 mm in the center of both UA and PS specimens- were benchmarked with FEM simulations with the goal of assessing whether the proposed specimen geometries were featuring the anticipated UA and PS strain path conditions in such sub-region of interest.

The tensile tests were simulated via FEM using LS-Dyna software. Fully integrated shell elements (ELFORM 16) were applied. The model for the PS specimens contained 10886 elements with a mesh size varying between 0.5 mm in the region of interest (middle part of the sample) to 1.7 mm on the specimen extremities. For the UA specimen, 7740 elements were employed, varying in size from 0.2 mm to 1 mm.

The material properties used for the simulations, including the Young's modulus and Poisson's ratio, are obtained from reference literature for polycrystalline pure copper, as their precise measurement is beyond the scope of this study. These properties are summarized in Table 6.

*MAT-PIECEWISE-LINEAR-PLASTICITY (*MAT-024) material model was used for both specimen geometries. This model features an elasto-plastic material representation, with an arbitrary stress-strain input curve which was obtained through experimental tensile tests (as de-
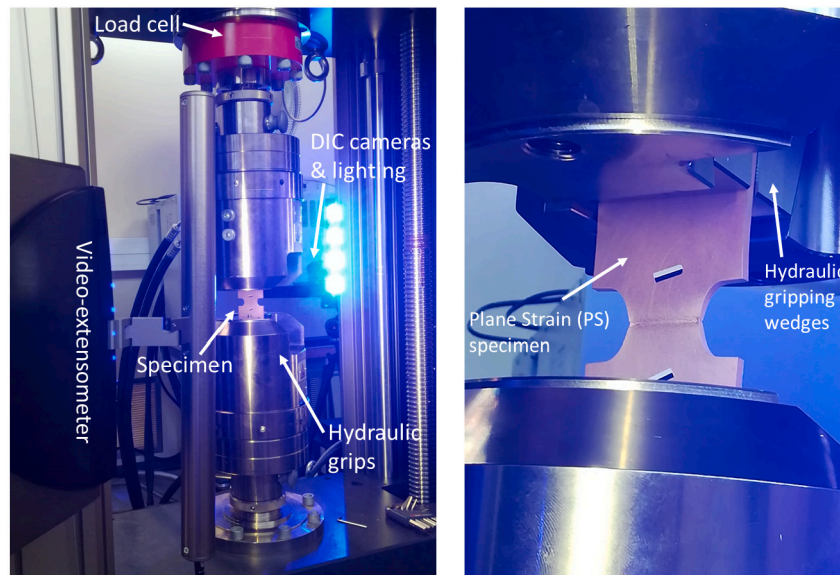
Fig. 4. Left image: Plane strain "PS" sample mounted on the hydraulic grips of the tensile testing machine with the video-extensometer pointing on one surface and the DIC cameras on the opposite surface. Right image: close-up view of the PS sample after rupture.

Table 4
Tensile test results for 2 mm thick Cu-OFE annealed sheets. * Values shown for $R_{p0.2}$ and $R_{p1.0}$ are the average from 4 specimens, the rest of parameters are the average of 2 specimens. Key: $R_{p0.2}$: Yield strength at 0.2% offset, $R_{p1.0}$: Yield strength at 1.0% offset, R_m: Ultimate tensile strength, A_g: Total elongation at maximum force, A_{25mm} = Elongation at break (on a 25 mm gauge length), $\frac{R_{p0.2}}{R_m}$ = Ratio of $R_{p0.2}$ to R_m, $n_{0.02-0.20 \text{ true strain}}$: Strain hardening exponent (calculated over true strain range from 0.02 to 0.20), $r_{20\% plastic strain}$: r-value (calculated at 20% engineering plastic strain).

Orientation w.r.t. sheet long direction	$R_{p0.2*}$ (MPa)	$R_{p1.0*}$ (MPa)	R_m (MPa)	A_g (%)
0 degrees	40.8 ± 0.2	48.2 ± 0.3	224.5 ± 0.4	41.1 ± 1.4
45 degrees	40.2 ± 0.2	47.6 ± 0.2	220.6 ± 0.3	43.4 ± 0.6
90 degrees	43.4 ± 1.6	51.1 ± 1.7	231.9 ± 0.0	37.6 ± 0.3

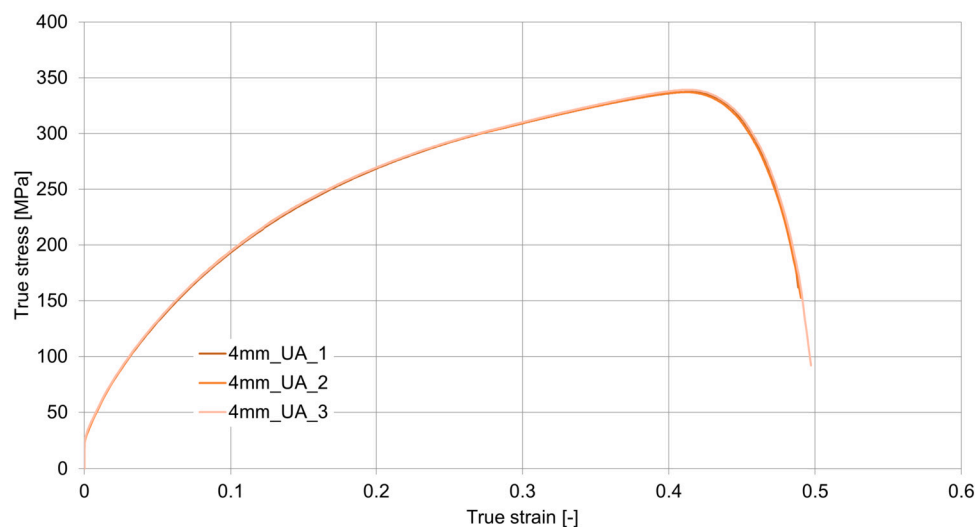| Orientation w.r.t. sheet long direction	A_{25mm} (%)	$R_{p0.2}/R_m$ (%)	$n_{0.02-0.20 true strain}$ (-)	$r_{20\% plastic strain}$ (-)
0 degrees	63.2 ± 1.6	18.1 ± 0.0	0.522 ± 0.001	0.85 ± 0.02
45 degrees	64.7 ± 0.2	18.2 ± 0.1	0.513 ± 0.002	0.99 ± 0.03
90 degrees	56.4 ± 1.5	18.3 ± 0.4	0.529 ± 0.004	0.81 ± 0.04

Fig. 5. True stress-strain curves of 4 mm thick specimens cut at 0° with respect to the sheet longest dimension. Three specimens were tested. Note that all curves are superposed denoting a high repeatability.
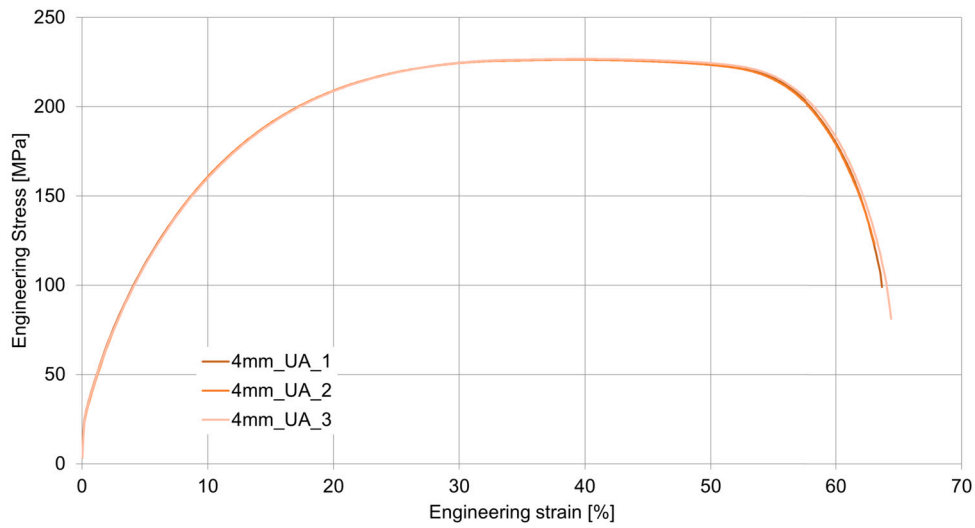
Fig. 6. Engineering stress-strain curves of 4 mm thick specimens cut at 0° with respect to the sheet long direction. Three specimens were tested.
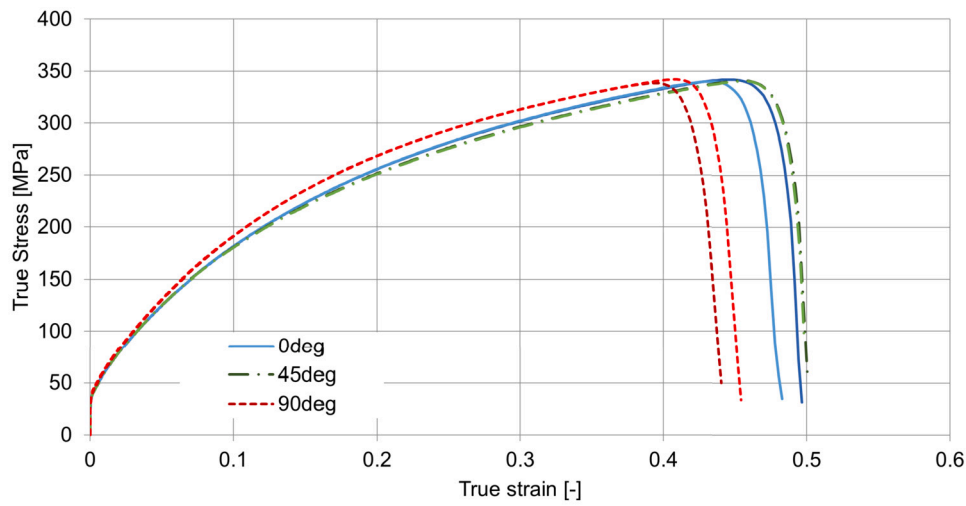

Fig. 7. True stress-strain curves of 2 mm thick specimens cut along three orientations (0, 45 and 90° with respect to the sheet longest direction). Two specimens for each orientation were tested.

Fig. 8. Engineering stress-strain curves of 2 mm thick specimens cut along three orientations (0, 45 and 90° with respect to the sheet longest direction). Two specimens for each orientation were tested.
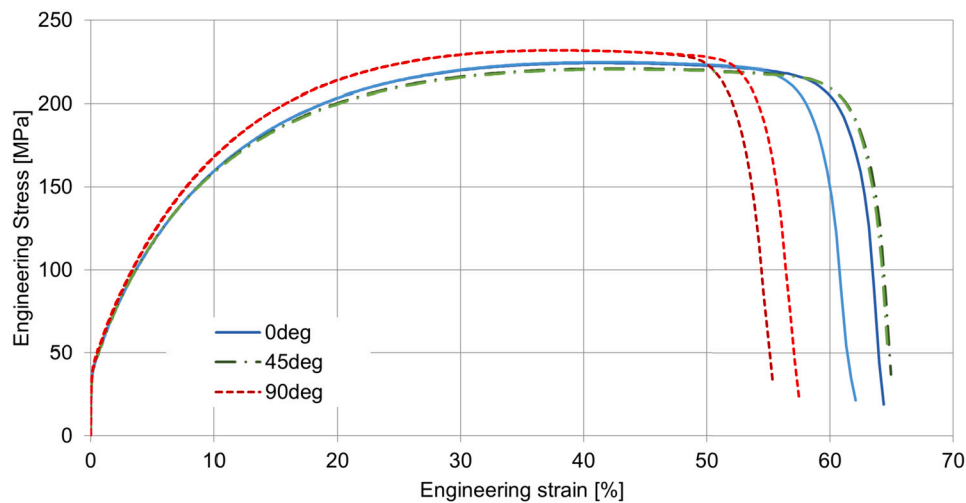
Table 5

Anisotropy values calculated according to the manual method of ISO-10113 and based on the r-values obtained from specimens tested at 0, 45 and 90 degrees orientation (shown in the previous table).

Weighted average plastic strain ratio	r_{avg}	0.91
Degree of planar anisotropy	Δr	−0.16

Table 6

Material properties used in the simulation.

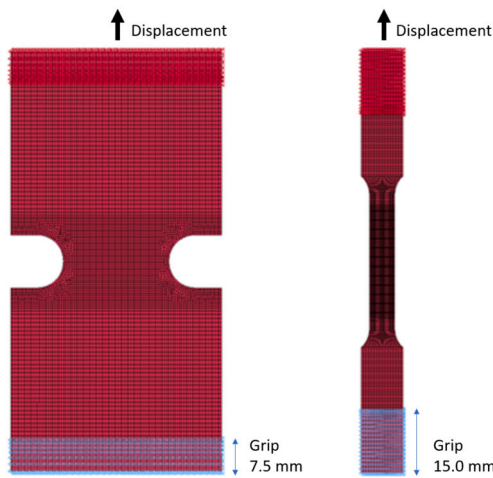| Density	Young's modulus	Poisson ratio
8894 kg/m^3	125 GPa [19]	0.34 [19]

Fig. 9. Boundary conditions and mesh for PS and UA specimens.

scribed in the Section 2.1). MAT-024 model applies isotropic material properties by default; Table 5 provides evidence supporting the validity of this assumption in the present case, as the obtained r-values (r_{avg} = 0.91, Δr = −0.16) indicate that Cu-OFE annealed sheets exhibit a rather isotropic behavior. In the simulation, a fixed boundary condition is defined on one extremity of the specimen, with a given grip length (specific for each specimen geometry) as implemented in the experiments. A vertical displacement, featuring the same grip length, is applied on the other extremity as shown in Fig. 9.

2.3. FLD construction

2.3.1. Failure by onset of necking: the forming limit curve (FLC)

Two different approaches were used for FLC calculation: experimental tensile tests on UA and PS specimens, and theoretical Forming Limit Curves based on Swift-Hill and Storen-Rice models.

Tensile tests on UA and PS specimens   DIC data (major ε_1 and minor ε_2 strain values for each x, y coordinate of the different sub-elements) was recorded and analyzed up to the frame (or time step) at which the strain field was discontinued due to a high distortion of the speckle pattern. This occurs at the most strained region the specimen, where the material has exceeded the onset of necking but ultimate rupture has not yet been reached. The subsequent analysis was performed with the last exploitable frame recorded before the above-mentioned loss of signal. With the acquired data, three criteria were applied for assessing the necking threshold: a less conservative criterion ("maximum strain"), a moderately conservative ("average strain") and more conservative criterion ("according to ISO 12004-2").

For the first one, the necking limit was set at the maximum recorded major true strain ε_1 (and the corresponding minor true strain ε_2) along a gauge placed on the necking region and with a length equal to the sheet thickness (thus 2 mm or 4 mm, respectively). For the second criterion, the limit was set at the computed average strain value along the same gauge length. These two criteria are assumed to be close to the manual approach proposed in [20], which is typically employed to record forming limit diagrams in metal-sheet workshops. For the third criterion a data post-processing routine was conceived and employed for the analysis of a strain profile to obtain $\varepsilon_1 - \varepsilon_2$ pairs; such routine has been adapted from [21], and discards the peak strains around the crack position. In this last criterion, the strain gauge length is coherently reduced (with respect to ISO 12004-2) to fit with the specimen geometry. Fig. 10 depicts the virtual gauges employed for the different criteria, in the case of a 4 mm thick uni-axial tensile specimen.

For UA specimens, each point (or $\varepsilon_1 - \varepsilon_2$ pair) in the FLC represents the average results for three virtual gauges (one line profile placed in the axis of three different specimens). For PS specimens, each point (or $\varepsilon_1 - \varepsilon_2$ pair) represents the average of six virtual gauges (three parallel line profiles spaced about 2 mm in the central region of two different specimens). All $\varepsilon_1 - \varepsilon_2$ pairs are plotted with a vertical and a horizontal error bar corresponding to one standard deviation (in the vertical direction for ε_1–axis and in the horizontal direction for ε_2–axis).

Theoretical forming limit curves   Two theoretical forming limit curves were calculated from the strain hardening index n, experimentally measured on the Cu-OFE samples (considering a power law formula for the flow stress–strain curve): the Swift-Hill's model, employed in [22] and [17], and the Storen-Rice's model, initially described by [23] and
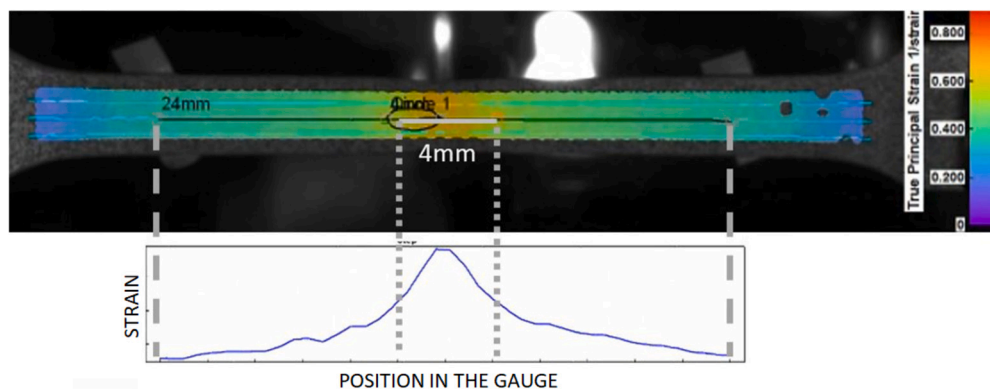

Fig. 10. Post-processed DIC image of a UA specimen during a test, with a schematic representation of a line profile (strain vs. position) containing a virtual gauge length of 4 mm used to compute the "maximum" and "average'" necking limit criteria, and a virtual gauge of 24 mm used to obtain the necking limit acc. to ISO 12004-2.

employed in the work of [22]. These models, which assume isotropic material behavior, are both based on bifurcation theory (which focus on the instability mechanisms at which a material transitions from a uniform deformation state to a localized necking) and are widely used in industry.

Swift-Hill's model

This model introduces the use of a parameter α as a ratio between minor and major strain.

$$\alpha = \varepsilon_2 / \varepsilon_1 \tag{1}$$

In this study, special focus is given to the zone of FLD between uniaxial tension and plane strain, which corresponds to negative minor strain, thus to $\alpha < 0$. For negative minor strains, the Hill's equations describing major (2) and minor (3) strain are the following:

$$\varepsilon_1 = \frac{n}{1+\alpha} \tag{2}$$

$$\varepsilon_2 = \frac{n\alpha}{1+\alpha} \tag{3}$$

Storen-Rice model

This model, foresees onset of necking for negative minor strain, as presented in equations (4) and (5).

$$\varepsilon_1 = \frac{\frac{n}{1+\alpha}}{\frac{1-n}{2} + \sqrt{\frac{(1+n)^2}{4} - \frac{n\alpha}{(1+\alpha)^2}}} \tag{4}$$

$$\varepsilon_2 = \frac{\alpha(\alpha^2 + n(2+\alpha)^2)}{2(2+\alpha)(1+\alpha+\alpha^2)} \tag{5}$$

The FLCs were calculated with strain hardening index $n = 0.535$ for 4 mm thick sheet and $n = 0.521$ for 2 mm thick sheet, respectively. Such n values are the averaged results obtained from the tensile tests of the UA specimens. In Fig. 18 and Fig. 19 both theoretical models are plotted together with FLC experimental points, based on the methodology explained in 2.3.1.

2.3.2. Failure by rupture: the fracture forming limit (FFL) and shear fracture forming limit (SFFL) curves

The typical application of FLD focuses on the onset of necking, as primary failure mechanism; the use of FLC thus usually suffices. For SRF considerations, though, the domain of micro and macro fracture becomes of interest, as surface quality is of utmost importance for SRF performance. In such case, SFFL and FFL curves should also be investigated. In this context, owing to the significant deformations and the resulting increased variability in values, a decision was made to adopt a more systematic and comparable calculation methodology, which was previously absent in the relevant literature. In order to streamline the process and enhance comprehension of the methods employed, the methodology can be primarily classified into two strain states: UA and PS.

In the UA case, the whole area of the specimen around the fracture is supposed to be at the expected strain path conditions ($\varepsilon_1 = -2\varepsilon_2$, considering an isotropic material) which allows the calculation of the strain components ε_2 (6) and ε_3 (7) from the observation of the fracture surface and, consequently, ε_1 by applying volume conservation (8), where ε_2 is the minor (plastic) true strain, w_0 is the initial width, w_f is the final width; ε_3 is the along-thickness (plastic) true strain, t_0 is the initial width, t_f is the final width; ε_1 is the major (plastic) true strain.

$$\varepsilon_2 = \ln\left(\frac{w_f}{w_0}\right) \tag{6}$$

$$\varepsilon_3 = \ln\left(\frac{t_f}{t_0}\right) \tag{7}$$

$$\varepsilon_1 = -(\varepsilon_2 + \varepsilon_3) \tag{8}$$

In this process, at least 15 measurements of both thickness and width were taken from the fractured surfaces. Based on the observation of
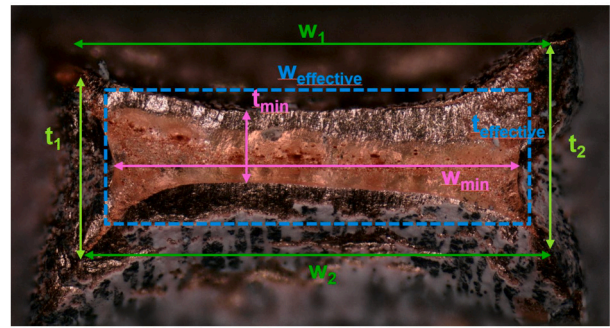

Fig. 11. Top view of a ruptured UA specimen (inspected using an optical microscope). Thickness and width measurement for estimating different points in the FFL.

the rupture surfaces, which are not perfectly rectangular, three distinct boundaries were established, which lead to three different fracture limits. The criterion referred as "effective limit" is determined following the guidelines of ASTM E8 standard, specifically concerning the measurements used to calculate the reduction in fracture area. This criterion enables to approximate the fracture surface to a parabolic shape in two dimensions, as outlined in equations (9)(10).

$$t_e = \frac{t_1 + 4t_{min} + t_2}{6} \tag{9}$$

$$t_{min} = \min t_i \tag{10}$$

where t_e is the "effective" thickness, t_1 and t_2 are, respectively, the thickness values on each side of the specimen, t_{min} is the minimum measured thickness. From "effective" thickness, the "effective" ε_3 can be calculated.

By applying the same process for "effective" width one could compute ε_2. And again applying conservation of volume, "effective" ε_1 can be calculated and in consequence the UA fracture point to include in the FLD.

To derive an upper limit, the minimum values for thickness and width were employed (this results in a less conservative threshold, as it considers highest levels of deformation). To draw a lower limit, the maximum values for thickness and width were used (this results in a more conservative threshold).

$$t_{max} = \max t_1, t_2 \tag{11}$$

A schematic representation of the measurements that can be taken on a fractured surface to derive the different fracture points is shown in Fig. 11.

However, in the case of PS it was observed, thanks to the DIC, that not all the specimen width exhibits plane strain state (this can be seen in Section 3.1). Namely, the outermost areas near the specimen edge display a non-negligible ε_2 (values larger than -0.1). Therefore, based also on DIC results, only the zone exhibiting quasi plane-strain which encompasses an 11 mm width (Fig. 12) was considered for the FFL estimation.

This zone was used to calculate the strain component ε_3 by measuring the thickness along its extent (Fig. 12). The value of ε_2 for determining the Fracture Forming Limit of PS specimens, has been assumed to be the same obtained for the FLC, as it is expected that the strain path evolves vertically from the necking limit to the ultimate failure in this condition (plane strain). After having ε_2 and ε_3, the ε_1 is obtained by volume conservation (Equation (8)). For the FFL estimation in PS condition, an average thickness was calculated and shown solely for the 4 mm-thick sheet, as the measurements for the 2 mm specimen were deemed insufficiently accurate.

The points (ε_1–ε_2 pairs) acquired through the measurement of the rupture surface of UA specimens are considered to be the intersection
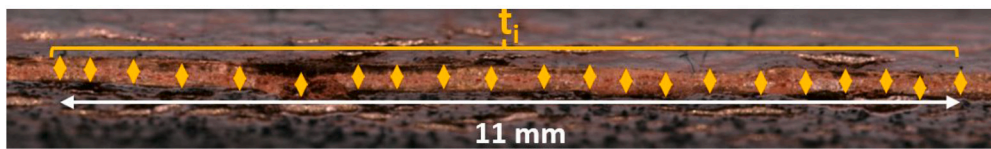
Fig. 12. Top view of the rupture surface of a PS specimen (inspected using an optical microscope) showing several thickness measurement points along the region of interest (about 11 mm) which has been submitted to plane strain deformation during the whole test.

Table 7
Slopes (*a*) used in Equation (12) to obtain SFFL curves.

Reference	Slope value
Jawale 2018 [24]	1.01
Correia 2016 [25]	1.17
Silva 2019 [26]	1.41

point between the SFFL and FFL curves; this interpretation leads to a conservative scenario in terms of failure. The FFL curve was determined through a linear regression of the points obtained from both UA and PS at fracture. To construct the SFFL curve, experimental data points for UA were combined with parameters from relevant literature, as listed in Table 7. The slopes used for the SFFL curve were derived from previous studies on copper sheets of varying thicknesses. Three slopes, with material properties closest to those in this study, were selected. Using the UA fracture limit point from this work and a slope, the parameter *b* was determined according to equation (12), positioning the SFFL curves in the FLD diagram.

$$\varepsilon_1 = a\varepsilon_2 + b \tag{12}$$

Obtained SFFL and FFL curves are presented in Section 3.3.

2.4. Surface roughness and hardness correlation with strain

Apart from the forming limit diagram, other material parameters can play a crucial role in the fabrication and operation of SRF components. For instance, surface quality (e.g. surface roughness, presence of voids open to the surface, presence of exogenous elements like hydrogen) is of paramount importance, as it can have an impact on the cavity performance. Deformation-induced roughness (the cause of the so called 'orange-peel') is therefore of interest for processes like hydroforming, where the cavity inner surface is not smoothened by a die (as is the case for spinning or deep drawing). In HF process, the cavity inner surface will feature zones with different roughness values that depend on the initial roughness conditions and grain size of the material, and on the level of strain reached locally during the process. Moreover, eventual defects like micro-cracks and pores on the surface of the cavities can also be detrimental to the cavity downstream fabrication processes and to its ultimate performance [27].

Hardness measurements can also be of interest for estimating the mechanical properties of parts produced by large deformation processes, and can be useful to benchmark FE simulations.

Measurements of hardness (HV 0.1 kgf) and average surface roughness (Ra) in function of strain are presented in this paragraph; as these represent complementary and useful information for the determination of the hydroforming process yield. Hardness measurements were performed with a micro-hardness testing machine and according to the ISO 6507–1 and roughness measurements were done with a contact profilometer and according to the ISO1997. Measurements were performed on ruptured UA specimens of both 2 mm and 4 mm thickness at various positions, namely 1 mm, 1.5 mm, 2 mm, 3 mm, 5 mm, 7 mm, 10 mm, and 15 mm from the rupture tip (see Fig. 13 and Fig. 14).

The objective was to establish a correlation between strain levels and the aforementioned parameters. Optical microscopy was utilized to measure the final width and thickness at each position. This allowed
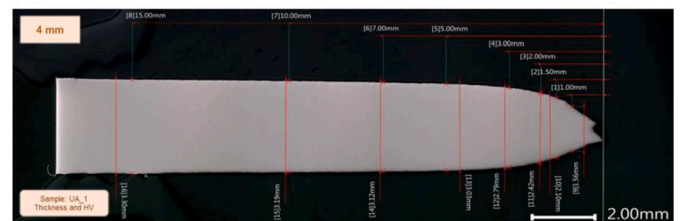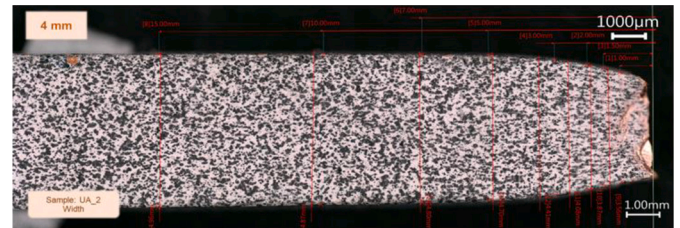

Fig. 13. Width, thickness, average surface roughness (Ra) and hardness were measured at 1 mm, 1.5 mm, 2 mm, 3 mm, 5 mm, 7 mm, 10 mm, and 15 mm from the rupture tip, on 4 mm thickness specimen. Top: Top surface view, Bottom: lateral cross-section view. Inspected with optical microscope.
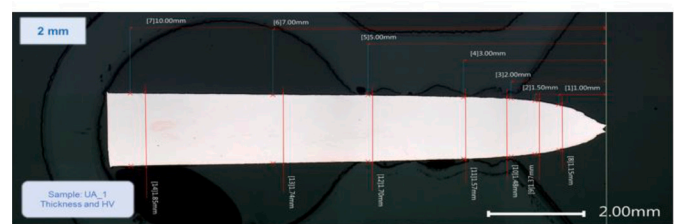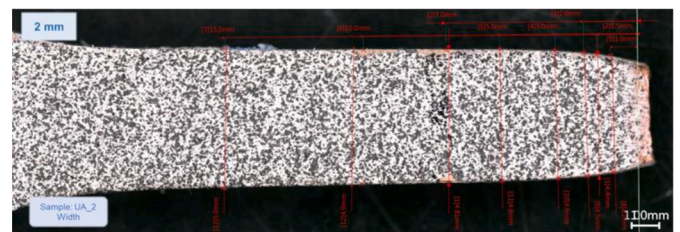

Fig. 14. Width, thickness, average surface roughness (Ra) and hardness were measured at 1 mm, 1.5 mm, 2 mm, 3 mm, 5 mm, 7 mm, 10 mm, and 15 mm from the rupture tip, on 2 mm thickness specimen. Top: Top surface view, Bottom: lateral cross-section view. Inspected with optical microscope.

to determine ε_2 and ε_3 and, subsequently, calculate ε_1 through volume conservation. It should be noted that this approach is a simplification for the calculation of ε_1, as assumptions of volume conservation may be less accurate for non-homogeneous plastic deformation.

For roughness analysis, each data point represents the average of two Ra values from roughness profiles taken from the top and bottom surfaces of the ruptured specimen. In terms of hardness, the points represent the average value derived from three measurement points at each position: 1/4, 1/2, and 3/4 of the specimen's thickness. The results are presented in Section 3.4.
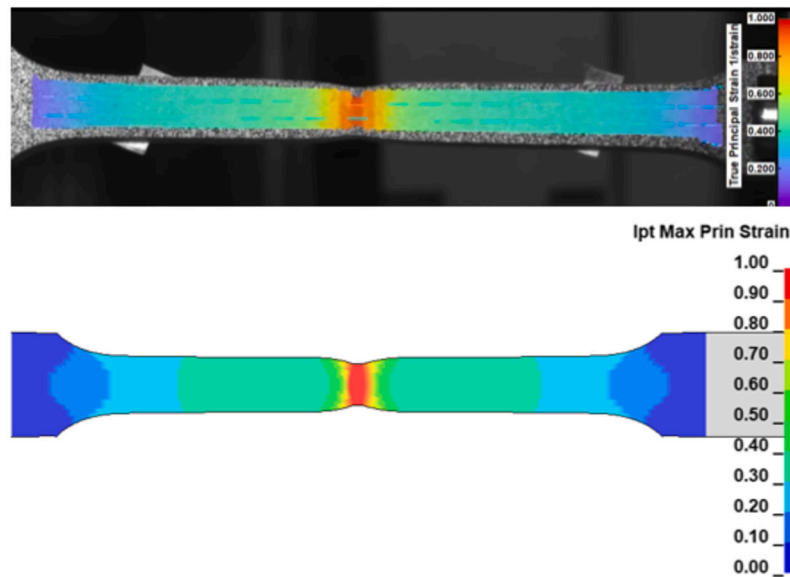
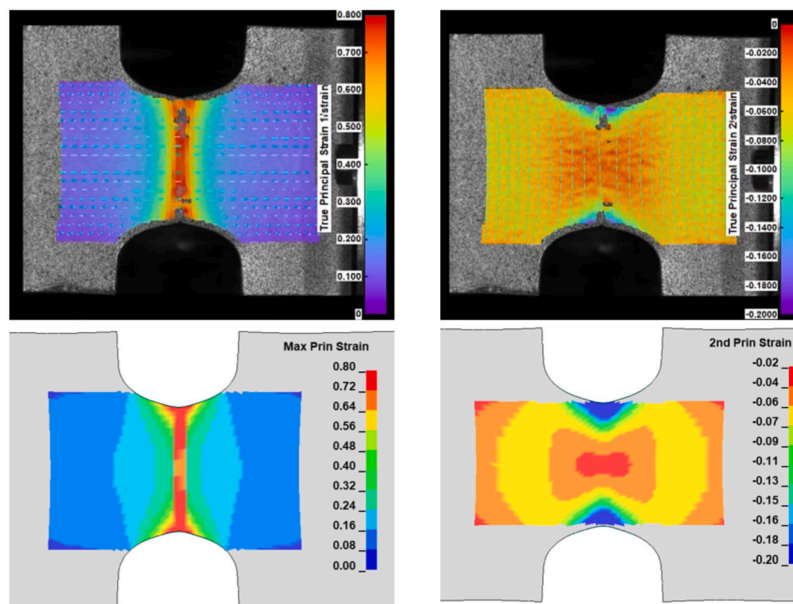**Fig. 15.** UA specimen DIC image (top) and simulation (bottom) comparison.

Fig. 16. PS specimen DIC image (top) and simulation (bottom) comparison. Comparison of ε_1 (left) and ε_2 (right).

The surface aspect of the UA specimens after rupture was examined with a scanning electron microscope SEM (FE-SEM ZEISS Sigma) using a secondary electron detector with accelerating voltage = 20 kV, working distance = 11 mm and aperture = 60 um as parameters.

3. Results and discussion

3.1. Benchmark of FE simulations and experimental results

The comparison between simulated and experimental tests with DIC is depicted in Fig. 15 (for UA specimen) and Fig. 16 (for PS specimen), showcasing the major strains (ε_1) and minor strains (ε_2) across the entire surface.

Additionally, the simulations are compared to experimental tests by evaluating a virtual gauge length of 4x4 mm placed on the region of maximum deformations in 4 mm thick specimens, as shown in Fig. 17.

For dog-bone shaped ASTM E8 subsize specimen, the uni-axial strain path was confirmed. Note that at major strains above 0.7, the strain path presents higher slope (it deviates gradually towards a plane strain condition until final rupture). For the PS specimen, a quasi-plane strain path was obtained (minor strain about -0.02) which is considered valid for the scope of the present study. A good matching between experimental and simulated strain paths is observed, therefore the geometry of both specimens was validated.

3.2. Forming limit curves

Figs. 18 and 19 depict the major (ε_1) and minor (ε_2) strain points for both UA and PS specimens, obtained through the implementation of each criterion as described in Section 2.3.1. The Forming Limit Curve (FLC) is defined, in the presented simplified method, by the straight line connecting the UA and PS points.

Also in Figs. 18 and 19 it can be observed that the FLC curves obtained with the 'Maximum' criterion, the 'Average' criterion and the criterion 'according to ISO 12004-2' are rather parallel with respect to each other and are ordered from less to more conservative, respectively.
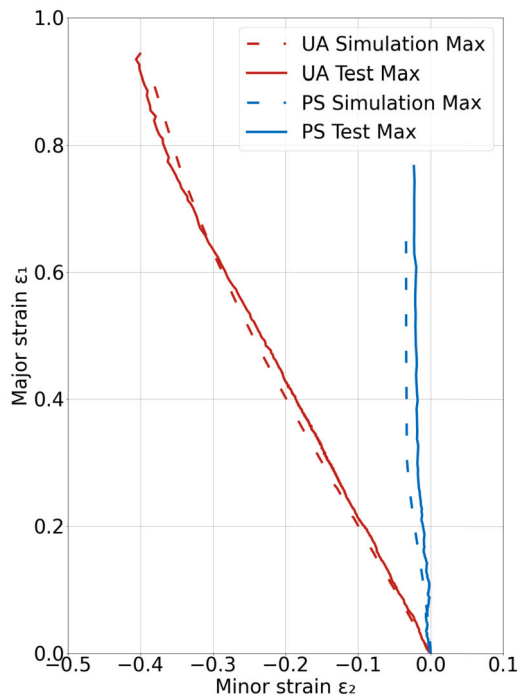
Fig. 17. Comparison of tensile test results for UA and PS specimens from experimental tests and finite element (FE) simulations, showing values of major and minor strains, ϵ_1 and ϵ_2, respectively.
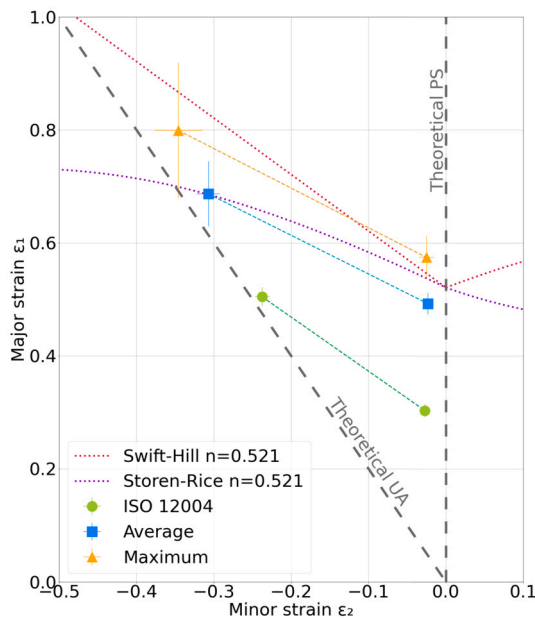

Fig. 18. Forming Limit Curves (FLCs) for 2 mm thick Cu-OFE specimens showing three criteria ranging from less to more conservative and a comparison with the Swift-Hill and Storen-Rice models.

Table 8 contains the linear equations derived from the experimental FLC curves, for the three above-mentioned criteria.

Concerning the 4 mm thick Cu-OFE sheet, the 'Average' curve matches well with the Storen-Rice theoretical model for both UA and PS cases, and also with Swift-Hill model in the PS zone; whereas the 'Maximum' curve matches better with the Swift-Hill model, especially close to the UA zone. For a 2 mm thick Cu-OFE sheet, the PS 'Maximum' limit fits into both Storen-Rice and Swift-Hill models; while for the UA limit, Storen-Rice fits to the 'Average' one.
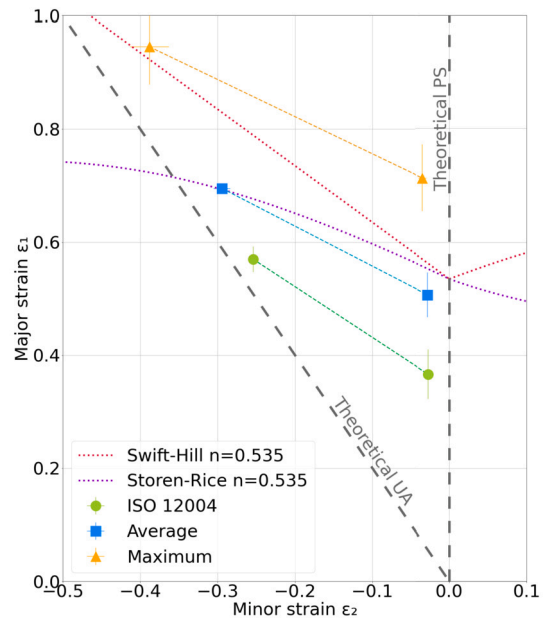

Fig. 19. Forming Limit Curves (FLCs) for 4 mm thick Cu-OFE specimens showing three criteria ranging from less to more conservative and a comparison with the Swift-Hill and Storen-Rice models.

Table 8
Summary of the forming limit curve equations (applicable to the 2nd quadrant) for 2 mm and 4 mm thick Cu-OFE annealed sheets, corresponding to the fitted linear regression of average UA and PS data points shown in Figs. 18 and 19, respectively.

Necking Criterion	2 mm thickness sheet	4 mm thickness sheet
Maximum strain (less conservative)	$\epsilon_1 = -0.70 * \epsilon_2 + 0.56$	$\epsilon_1 = -0.66 * \epsilon_2 + 0.69$
Average strain (moderately conservative)	$\epsilon_1 = -0.69 * \epsilon_2 + 0.47$	$\epsilon_1 = -0.71 * \epsilon_2 + 0.49$
ISO 12004 (more conservative)	$\epsilon_1 = -0.95 * \epsilon_2 + 0.28$	$\epsilon_1 = -0.90 * \epsilon_2 + 0.34$

When calculating a limit with ISO 12004-2 or 'Maximum' criterion, the obtained FLCs for 4 mm and 2 mm thick sheets show increased formability with increased thickness. While the curve obtained with 'Average' criterion results in similar formability, regardless of the thickness of the metal sheet.

At the left region from the uni-axial strain (zone close to pure shear strain path) is expected that the failure will not occur by thinning (i.e. necking) and the sample will fail directly by rupture. At the above-mentioned zone the FLC could be considered flat (similar to Storen-Rice model) for a conservative approach or be extended with the same slope from the UA-PS line, thus in agreement with Swift-Hill model.

The Forming Limit Curves (FLC) reported in the literature [16] for Cu-OFE annealed sheets (C12000) of low thickness (0.66 mm) fall between the curves labeled 'Average' and 'Maximum' in the present work. This might be due to the fact that the curve from [16] was built with strains derived from fiducial markings etched onto the surface of samples prior to deformation, thus capturing part of the localized plastic deformation, as our two less conservative criteria do. We believe that, to perform moderately conservative forming operations on thick sheets while avoiding the initiation of local necking, one should target strain levels that fall between the curves labeled 'ISO 12004' and 'Average'.

While this study focuses on the annealed temper state to maximize formability and reduce intermediate annealing steps, it is important to note that harder temper states, such as quarter-hard, half-hard, or hard, may be used for applications requiring lower or moderate forming (or no forming at all). These temper states preserve grain size and material strength (Rp0.2, Rm), which can be beneficial for maintaining the

Fig. 20. Forming Limit Diagram for Cu-OFE 2 mm thick sheet consisting in the FLC curves (failure by necking) together with the SFFL (failure by fracture in shear) based on experimental fracture points and slopes from [24], [25], [26].
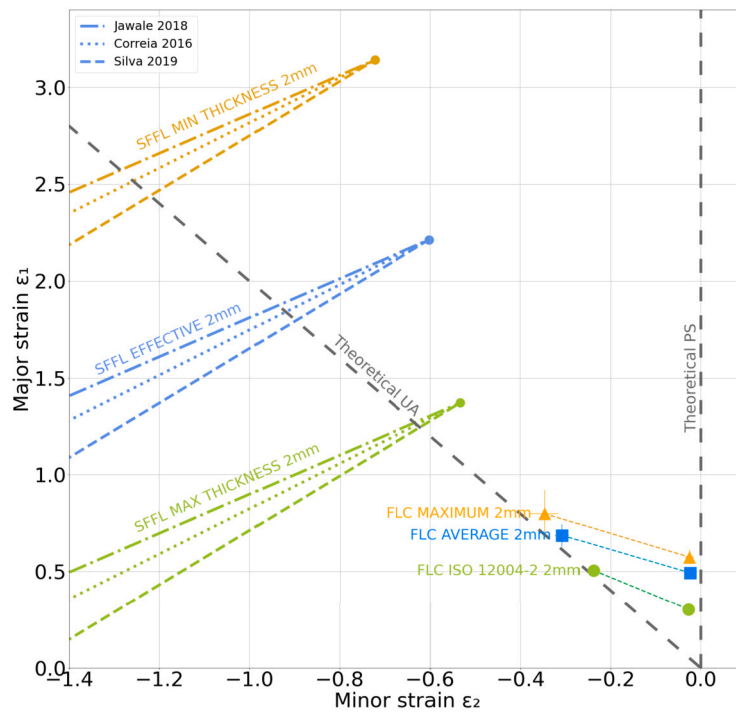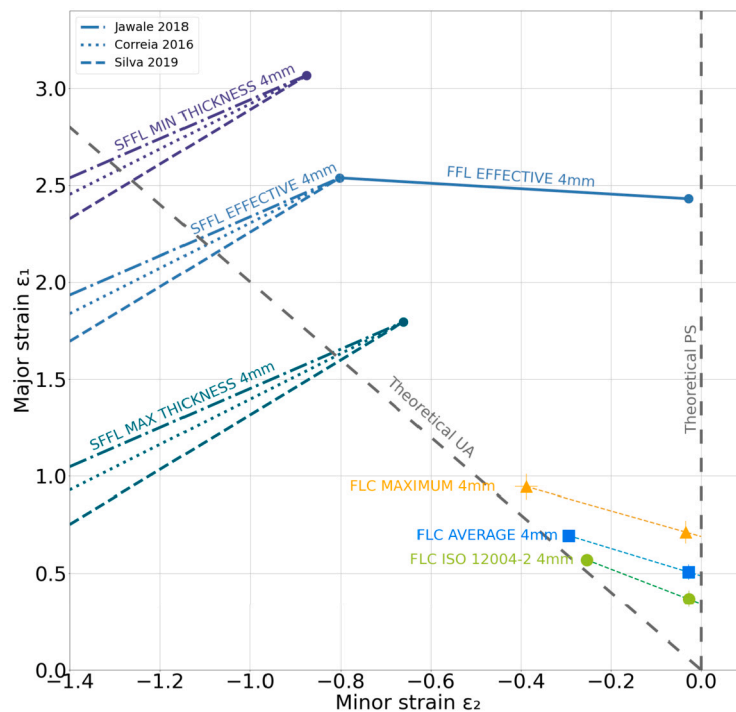

Fig. 21. Forming Limit Diagram for Cu-OFE 4 mm thick sheet consisting in the FLC curves (failure by necking) together with the FFL (failure by fracture) and the SFFL (failure by fracture in shear) based on experimental fracture points and slopes from [24], [25], [26].

structural integrity of some parts. Dedicated FLDs for these harder temper states would be required in such cases but are beyond the scope of this study.

3.3. Fracture limits: SFFL and FFL

The obtained SFFL and FFL curves, shown in Fig. 20 and Fig. 21 for 2 mm and 4 mm thick sheet respectively, demonstrate that an increase

in fracture strain limits can be expected as sheet thickness increases: the limits obtained for 4 mm thick sheets surpass those for 2 mm thick sheets.

As explained in Section 2.3.2, it is important to acknowledge that the presented FFL and SFFL limits were derived using three methodologies that, in turn involve the measurement of distances. These methodologies lead to less conservative, moderately conservative, and more conservative fracture limits. The three limits show significant differences, that
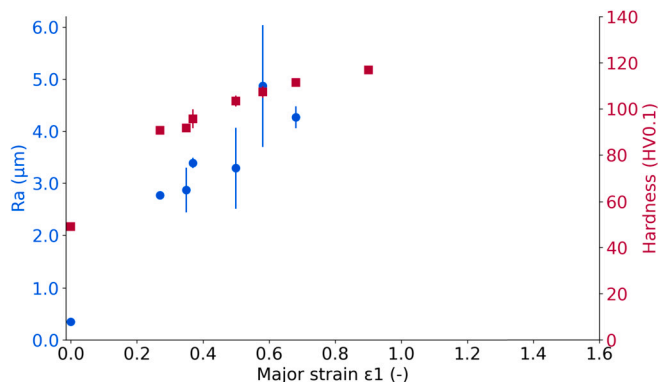
Fig. 22. Average surface roughness Ra and hardness HV0.1 vs. major (plastic) true strain for 2 mm thick specimen; initial grain size 52 μm. Error bars represent one standard deviation for hardness and half of the range for Ra.
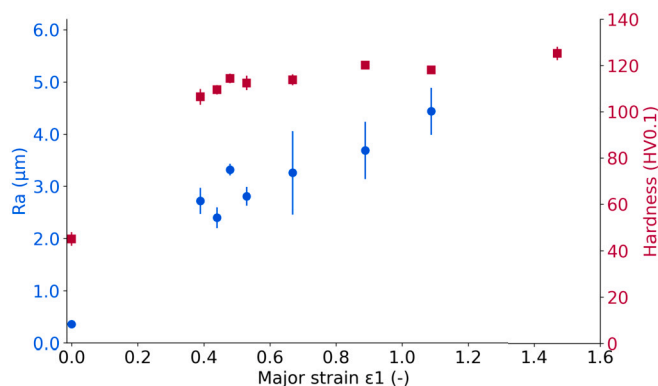

Fig. 23. Average surface roughness Ra and hardness HV0.1 vs. major (plastic) true strain for 4 mm thick specimen; initial grain size 44 μm. Error bars represent one standard deviation for hardness and half of the range for Ra.

arise from the intrinsic methodology employed. The estimated uncertainty of strains calculated from measurement of distances with optical microscope images at 20x magnification (resolution 0.01 mm or better) is less than 5%. The curves labeled "Jawale 2018", "Correia 2016", "Silva 2019" are extracted from literature and represent typical trends for shear fracture limits of pure Cu sheet. Together with the UA fracture points measured in this work, these references allow to estimate the slope and position of the SFFL curves.

3.4. Surface roughness and hardness correlation with strain

The resulting average values of hardness and surface roughness were plotted against the true major strain ε_1, as depicted in Fig. 22 and Fig. 23 for 2 mm and 4 mm specimens, respectively.

Based on error propagation methods, the estimated uncertainty in the calculated strain ε_1 (X axis), derived from measurements of thickness and width of specimens with a precision of 0.01 mm, ranged from 0.53% for the highest recorded strain values ($\varepsilon_1 = 1.5$) to 2.51% for the lowest strain values ($\varepsilon_1 = 0.27$).

It can be observed that the initial values (in annealed state, i.e. zero strain) are close to 45 HV for hardness, and about 0.4 μm concerning average surface roughness (Ra). After rupture, at a true major strain $\varepsilon_1 = 0.4$ (corresponding to a distance significantly far from the crack) the 4 mm thick specimens shows a hardness slightly above 100 HV and a surface roughness of about Ra = 2.5 μm; while for 2 mm thick specimens the values are of about 90 HV and Ra = 3 μm. The most extreme values measured close to the crack tip have been about 120 HV and Ra = 4.5 μm for the 4 mm thick specimens and slightly under 120 HV and Ra = 4 to 5 μm for 2 mm thick specimens. Is therefore observed

that both hardness and Ra increase significantly from $\epsilon_1 = 0$ to about $\epsilon_1 = 0.3$–0.4 (corresponding to the measured Ag, i.e. elongation at the maximum force, or maximum homogeneous deformation). For higher strain values, hardness evolves in a more asymptotic manner, while average roughness (Ra) appears to continue increasing. However, due to the measured scatter in roughness, it is difficult to establish a clear trend. Note that the maximum major true strain measured at 1 mm from the tip is higher for 4 mm thick sheets (about $\epsilon_1 = 1.50$) than for 2 mm thick sheets (about $\epsilon_1 = 0.90$).

The differences observed between 2 mm and 4 mm thick specimens can be due to several factors like: initial grain size, exact necking position, operator discretion at measuring the distance to the crack tip and the plastic material flow during the test, which will presumably be influenced by the width-to-thickness aspect ratio.

Given the established correlation between the major strain value and the analyzed parameters (surface roughness and hardness), it is envisaged to conduct additional research to explore their interdependence. Specifically, it is advisable to include strain values within the homogeneous plastic deformation regime as well as study the relationship for different strain paths.

Fig. 24 shows the evolution of surface morphology and roughness in 4 mm thick UA Cu-OFE specimens at different zones (corresponding to different strain levels). The as-received condition (Fig. 24a) has a smooth surface with $R_a = 0.4\,\mu m$. At 10 mm from the crack ($\epsilon_1 \approx 0.44$) (Fig. 24b), roughness increases to $R_a \approx 2.4\,\mu m$. Closer to the crack, at 1.5 mm distance ($\epsilon_1 \approx 1.09$) (Fig. 24c), roughness increases at $R_a \approx 4.4\,\mu m$. The fracture tip (Fig. 24d) shows severe deformation with significant surface irregularities, and a close-up (Fig. 24e) reveals certain "waviness" due to differential plastic deformation of the grains, together with some surface voids and slip bands. These results, that are complementary to the results of Figs. 22 and 23, illustrate the increase in roughness and appearance of deformation features (including surface damage) with strain.

In addition to the forming limit diagram presented in this paper, it is known other material parameters that evolve with strain are of paramount importance for SRF applications.

Therefore, the concept of 'SRFLD' can be introduced. The 'SRFLD' shall be an extended version of the forming limit diagram, with special focus on SRF applications, and embedding additional data and mechanisms of interest that evolve in function of strain, such as: surface roughness, onset of material defects (pores, micro-cracks) [28], [29] and eventually extending to other relevant information like thickness reduction, and hardness evolution. All of these variables may be plotted in FLD-like diagrams (with ϵ_1 as y-axis and ϵ_2 as x-axis), in order to visualize their evolution in function of the strain path (uni-axial, plane-strain, pure-shear, etc). Dedicated studies, to populate such 'SRLFD' data, are planned by the authors and are undergoing.

4. Conclusion and future developments

In the context of optimizing the manufacturing process of SRF cavities for particle accelerators, this study presents a comprehensive material characterization of annealed Cu-OFE sheets of 2 mm and 4 mm thickness including: grain size, hardness, surface roughness and tensile mechanical properties, together with the construction of a simplified Forming Limit Curve (FLC) and Fracture Forming Limits (FFL and SFFL, respectively).

The FLC presented in this work, which serves as a crucial indicator for the onset of necking of annealed Cu-OFE submitted to large deformation following different linear strain paths, is determined using three distinct criteria: 'maximum', 'average', and 'according to ISO 12004-2'. These criteria establish a range of necking thresholds, from less conservative to more conservative, respectively. It can be noted that the 'average' method proves to be a good match with the Storen-Rice theoretical model. This estimation can be applied to both 4 mm and 2 mm thick sheets.
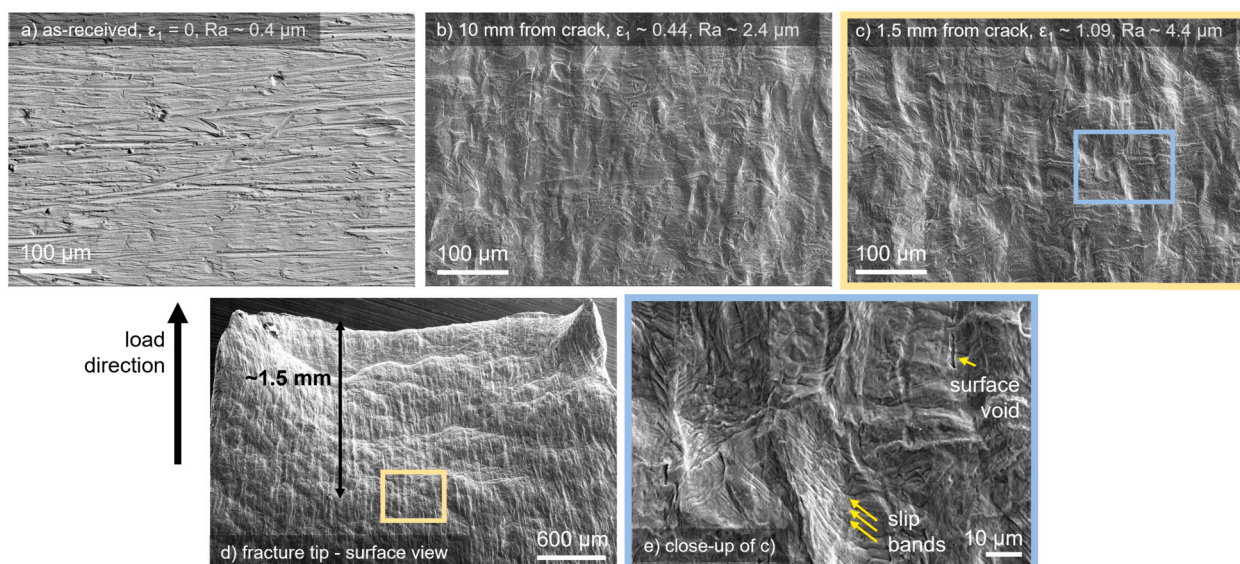
Fig. 24. SEM images of the surface aspect at different zones (corresponding to different strain) of a ruptured UA specimen. Magnification values refer to original magnification: a) as-received condition 200x, b) at 10 mm from fracture tip 200x, c) at 1.5 mm from fracture tip 200x, d) overview of the fracture tip 32x, e) close up view of image c) 1000x.

The Fracture Forming Limit (FFL) for the 4 mm thick sheet was derived from the same experimental tests used for the FLC. The SFFL limits for both 4 mm and 2 mm thick sheets were determined by combining experimental data with relevant literature information from similar materials. It should be noted that both the SFFL and FFL limits were obtained using a much simpler and less resource-consuming method, if compared to standard approaches like Nakazima or Marciniak tests, although they cover only the 2nd quadrant of the FLD. The studies conducted enable the development of a failure model for Cu-OFE sheets, which can be widely employed to ultimately estimate the feasibility of various large deformation processes, also through numerical simulations.

We introduced the concept of the 'SRFLD', an extended version of the forming limit diagram (FLD) tailored for SRF applications, which shall incorporate additional strain-evolving material parameters such as surface roughness, the onset of surface defects, hardness or thickness reduction, to provide a more comprehensive understanding of material behavior under different strain paths and strain levels.

The preliminary FE analyses conducted by the authors, presented in [30], show how the tubular hydroforming process of the copper substrate for superconducting RF cavities exhibits a linear strain path that increases monotonically, similar to a uniaxial (UA) path. The results obtained from the present work are thus adequate for the feasibility assessment of SRF cavity substrates fabrication by hydroforming, since the relevant manufacturing process will be encompassed by the obtained FLCs. In future work, the outcomes presented in this study will be verified through experimental hydroforming trials on several components and the results will be benchmarked against finite element (FE) simulations.

CRediT authorship contribution statement

Adrià Gallifa-Terricabras: Writing – review & editing, Writing – original draft, Validation, Methodology, Investigation, Formal analysis, Data curation, Conceptualization. **Joanna Sylwia Swieszek:** Writing – review & editing, Writing – original draft, Methodology, Investigation, Data curation, Conceptualization. **Dorota Smakulska:** Writing – review & editing, Writing – original draft, Visualization, Methodology, Investigation, Formal analysis, Data curation, Conceptualization. **Berta Ruiz-Palenzuela:** Writing – review & editing, Writing – original draft, Methodology, Investigation, Formal analysis, Concep-

tualization. **Marco Garlaschè:** Writing – review & editing, Writing – original draft, Validation, Supervision, Resources, Methodology, Investigation, Conceptualization.

Declaration of competing interest

The authors declare that they have no known competing financial interests or personal relationships that could have appeared to influence the work reported in this paper.

Data availability

Data will be made available on request.

Acknowledgements

Appendix A. Supplementary material

Supplementary material related to this article can be found online at https://doi.org/10.1016/j.matdes.2024.113191.

References

[1] Cristoforo Benvenuti, Superconducting coatings for accelerating rf cavities: past, present, future, Part. Accel. 40 (CERN-MT-DI-91-6) (1991) 43–57.

[2] Michael Benedikt, Volker Mertens, Francesco Cerutti, Werner Riegler, Thomas Otto, Davide Tommasini, Laurent Jean Tavian, Johannes Gutleber, Frank Zimmermann, Michelangelo Mangano, et al., Fcc-hh: the hadron collider: future circular collider conceptual design report volume 3, Eur. Phys. J. Spec. Top. 228 (CERN-ACC-2018-0058) (2018) 851–858.

[3] E.A. Ilyina, Guillaume Rosaz, Josep Busom Descarrega, Wilhelmus Vollenberg, A.J.G. Lunt, Floriane Leaux, Sergio Calatroni, W. Venturini-Delsolaro, Mauro Taborelli, Development of sputtered nb3sn films on copper substrates for superconducting radiofrequency applications, Supercond. Sci. Technol. 32 (3) (2019) 035002.

[4] M. Arzeo, F. Avino, S. Pfeiffer, G. Rosaz, M. Taborelli, L. Vega-Cid, W. Venturini-Delsolaro, Enhanced radio-frequency performance of niobium films on copper substrates deposited by high power impulse magnetron sputtering, Supercond. Sci. Technol. 35 (5) (apr 2022) 054008, https://doi.org/10.1088/1361-6668/ac5646.

[5] Guillaume Rosaz, Aleksandra Bartkowska, Carlota P.A. Carlos, Thibaut Richard, Mauro Taborelli, Niobium thin film thickness profile tailoring on complex shape substrates using unbalanced biased high power impulse magnetron sputtering, Surf. Coat. Technol. (ISSN 0257-8972) 436 (2022) 128306, https://doi.org/10.1016/j.surfcoat.2022.128306, https://www.sciencedirect.com/science/article/pii/S0257897222002274.

[6] S. Aliasghari, E. Avcu, P. Skeldon, R. Valizadeh, B. Mingo, Abrasion resistance of a nb3sn magnetron-sputtered coating on copper substrates for radio frequency superconducting cavities, Mater. Des. (ISSN 0264-1275) 231 (2023) 112030, https://doi.org/10.1016/j.matdes.2023.112030, https://www.sciencedirect.com/science/article/pii/S0264127523004458.

[7] M. Ghaemi, A. Lopez-Cazalilla, Kostas Sarakinos, G.J. Rosaz, C.P.A. Carlos, S. Leith, S. Calatroni, M. Himmerlich, F. Djurabekova, Growth of nb films on cu for superconducting radio frequency cavities by direct current and high power impulse magnetron sputtering: a molecular dynamics and experimental study, Surf. Coat. Technol. 476 (2024) 130199.

[8] Claude Hauviller, Fully hydroformed rf cavities, http://cds.cern.ch/record/196374, 1990.

[9] Takeo Fujino, S. Koide, H. Inoue, A. Kubota, Masaaki Ono, K. Saitô, S. Noguchi, E. Kako, T. Shishido, Status of the seamless l-band cavity fabrication at kek, Technical report, SCAN-9605111, 1996.

[10] P. Kneisel, V. Palmieri, Development of seamless niobium cavities for accelerator applications, in: Proceedings of the IEEE Particle Accelerator Conference, vol. 2, 1999, pp. 943–945.

[11] W. Singer, Seamless/bonded niobium cavities, in: Proceedings of 12th International Workshop on RF Superconductivity, 2005.

[12] A. Amorim Carvalho, Jean-Pierre Brachet, Bartosz Bulat, Ofelia Capatina, Alessandro Dallocchio, Marco Garlaschè, Manuele Narduzzi, Laurent Prever-Loiri, Simulation of niobium sheets forming for accelerating cavities: challenges and achievements, in: LS-DYNA Forum, 2016.

[13] A. Amorim Carvalho, S. Barrière, J. Brachet, B. Bulat, R. Calaga, E. Cano-Pleite, O. Capatina, T. Capelli, A. Dallocchio, M. Garlaschè, et al., Advanced Design of Tooling for Sheet-Metal Forming Through Numerical Simulations in the Scope of Srf Crab Cavities at Cern, AIP Conference Proceedings, vol. 2113, AIP Publishing LLC, 2019, p. 100008.

[14] Muammer Koc, Hydroforming for Advanced Manufacturing, Woodhead Publishing, ISBN 978-1-84569-328-2, 2008.

[15] I. Numisheet Benchmarks, Virtual forming limit curves, in: 7th International Conference and Workshop on Numerical Simulation of 3D Sheet Metal Forming Processes, 2008.

[16] Joseph R. Davis, et al., Copper and Copper Alloys, ASM International, 2001.

[17] Jean-Francois Croteau, Single crystal and polycrystalline niobium and ofe copper for sfr cavities applications: mechanical characterization at low to high strain rates and microstructural investigations 231 (2021) 68.

[18] Matthias Lenzen, Marion Merklein, Improvement of numerical modelling considering plane strain material characterization with an elliptic hydraulic bulge test, J. Manuf. Mater. Proces. 2 (6) (2018) 01, https://doi.org/10.3390/jmmp2010006.

[19] J. Crane, F. Mandigo, Forming of Copper and Copper Alloys, Forming and Forging, ASM Handbook, ASM International, ISBN 9780471154327, 1988.

[20] ISO 12004-1:2020, Metallic materials – sheet and strip – determination of forming limit curves – part 1: Measurement and application of forming limit diagrams in the press shop, Standard, International Organization for Standardization, 2020.

[21] ISO 12004-2:2021, Metallic materials – sheet and strip – determination of forming limit curves – part 2: Determination of forming limit curves in the laboratory, Standard, International Organization for Standardization, 2021.

[22] Ruiqiang Zhang, Zhutao Shao, Jianguo Lin, A review on modelling techniques for formability prediction of sheet metal forming, Int. J. Lightweight Mater. Manuf. (ISSN 2588-8404) 1 (3) (2018) 115–125.

[23] S. Stören, J.R. Rice, Localized necking in thin sheets, J. Mech. Phys. Solids (ISSN 0022-5096) 23 (6) (1975) 421–441.

[24] Kishore Jawale, Jose Ferreira Duarte, Ana Reis, Maria Beatriz Silva, Characterizing fracture forming limit and shear fracture forming limit for sheet metals, J. Mater. Process. Technol. (2018).

[25] Joana Margarida, Esturrado Correia, CaracterizaÇÃo dos limites de enformabilidade para chapa metÁlica de cobre, Master's thesis, Instituto Superior Técnico, University of Lisbon, 2016, Dissertação para obtenção do Grau de Mestre em Engenharia Mecânica.

[26] Maria Beatriz Silva, Joao P. Magrinho, Luis Reis, Paulo A.F. Martins, Formability limits, fractography and fracture toughness in sheet metal forming, in: Materials 2019, 2019.

[27] H. Padamsee, J. Knobloch, T. Hays, RF Superconductivity for Accelerators, Wiley Series in Beam Physics and Accelerator Technology, Wiley, ISBN 9780471154327, 1998, https://books.google.ch/books?id=2leaQgAACAAJ.

[28] S. Aliasghari, P. Skeldon, X. Zhou, A. Gholinia, X. Zhang, R. Valizadeh, C. Pira, T. Junginger, G. Burt, P.J. Withers, X-ray computed tomographic and focused ion beam/electron microscopic investigation of coating defects in niobium-coated copper superconducting radio-frequency cavities, Mater. Chem. Phys. (ISSN 0254-0584) 273 (2021) 125062, https://doi.org/10.1016/j.matchemphys.2021.125062, https://www.sciencedirect.com/science/article/pii/S0254058421008452.

[29] Jianwei Li, Chaogang Ding, Wanji Chen, Debin Shan, Bin Guo, Jie Xu, Strain localization and ductile fracture mechanism of micro/mesoscale deformation in ultrafine-grained pure copper, Mater. Des. 229 (2023) 111873.

[30] Joanna Sylwia Święszek, Marco Garlaschè, Dorota Smakulska, Adria Gallifa-Terricabras, Simulations and characterization of fabrication processes for srf, in: 6th CERN SRF Workshop, Geneva, CERN, February 2023.